Effects of 3*d* Electron Configurations on Helium Bubble Formation and Void Swelling in Concentrated Solid-Solution Alloys

Yanwen Zhang [a,b,*], Xing Wang [c], Yuri N. Osetsky [a], Yang Tong [a], Robert Harrison [d], Stephen E. Donnelly [d], Di Chen [e], Yongqiang Wang [e], Hongbin Bei [a], Brian C. Sales [a], Karren L. More [c], Pengyuan Xiu[f], Lumin Wang [f], and William J. Weber [b,a]

[a] *Materials Science and Technology Division, Oak Ridge National Laboratory, Oak Ridge, TN 37831, USA*

[b] *Department of Materials Science and Engineering, The University of Tennessee, Knoxville, TN 37996, USA*

[c] Center for Nanophase Materials Sciences, Oak Ridge National Laboratory, Oak Ridge, TN, 37832, USA

[d] *School of Computing and Engineering, University of Huddersfield, Huddersfield, HD1 3DH, UK*

[e] *Materials Science and Technology Division, Los Alamos National Laboratory, Los Alamos, NM, USA*

[f] *Department of Nuclear Engineering and Radiological Sciences, University of Michigan, Ann Arbor, MI 48109, USA*

Abstract: Elemental specific chemical complexity is known to play a critical role in microstructure development in single-phase concentrated solid-solution alloys (SP-CSAs), including both He bubble formation and irradiation-induced void swelling. While cavity formation and evolution under ion irradiation at elevated temperature are complex nonequilibrium processes, chemical effects are revealed at the level of electrons and atoms herein in a simplified picture, using Ni and a special set of Ni-based SP-CSAs composed of 3*d* transition metals as model alloys. Based on Ni and model alloys with minimized variables (e.g., atomic mass, size, and lattice structure), we discuss the effects of chemically-biased energy dissipation, defect energetics, sluggish diffusion, and atomic transport on cavity formation and evolution under both self-ion Ni irradiation and He implantation. The observed difference in microstructure evolution is attributed to the effects of *d* electron interactions in their integrated ability to dissipate radiation energy. The demonstrated impact of alloying 3*d* transition metals with larger differences in the outermost electron counts suggests a simple design strategy of tuning defect properties for improved radiation tolerance in structural alloys.

Keywords: concentrated solid-solution alloys; defect dynamics; microstructure evolution; ion irradiation; Cavity formation

[*] Corresponding author: zhangy1@ornl.gov, Oak Ridge National Laboratory, Ph: 865-574-8518, Fax: 865-241-3650

.

1. Introduction

Alloys consisting of two or more metallic elements (i.e., nickel [Ni] or iron [Fe] with limited amounts of other elements) have been intensively investigated to achieve superior properties, such as mechanical strength and radiation tolerance, as well as corrosion resistance. Helium (He) can be produced from (n, α) reactions or α-decay of fission products or the fusion of deuterium with tritium (releasing a 14.1 MeV neutron and a 3.5 MeV He nucleus) and has little solubility in alloys. The presence of He atoms leads to nucleation and growth of cavities. The formation and evolution of cavities in fission and fusion environments play a significant role in the performance of structural alloys, as the aggregation of vacancies and He atoms results in macroscopic damage and swelling that can significantly degrade an alloy's properties under irradiation.[1]

Recently, researchers have shown that chemical complexity resulting from the presence of several major elements in single-phase concentrated solid-solution alloys (SP-CSAs) can provide superior properties that may not be expected in diluted alloys, such as low-temperature ductility[2] and improved radiation performance.[3-7] Studies have revealed unique defect properties in SP-CSAs that affect radiation-induced microstructural evolution and suppress cavity formation and growth. Yang et al. show that, in Ni and binary alloys, the average size of defect clusters decreases as the solute atomic volume size factor increases, and oversized solutes act as strong trapping sites for interstitials.[8,9] Significant reduction in volume swelling by nearly two orders of magnitude under high-temperature high-fluence irradiation was achieved by increasing chemical complexity in SP-CSAs.[6] Whereas Ni and NiCo exhibit large voids in the irradiated region, in front of interstitial-type dislocation structures, other SP-CSAs with different alloying elements show interstitial-type dislocation loops in the irradiated region, trailed by smaller voids distributed beyond the end of the ion range. Enhanced swelling resistance is attributed to tailoring of interstitial defect cluster motion, from a long-range one-dimensional (1D) mode in pure Ni and NiCo to short-range three-dimensional (3D) motion or nearly complete immobilization in NiFe and in some more complex SP-CSAs.[6,10] The 3D motion of interstitial clusters is believed to increase the vacancy-interstitial recombination rate, therefore reducing void swelling in complex alloys.

In addition to the difference in irradiation-induced void formation, suppressed He bubble growth in SP-CSAs is also reported.[11-13] Studies[11,12] have demonstrated that vacancy and interstitial migration energies can be tailored through careful selection of alloying elements and composition; and closer migration energies of interstitials and vacancies promote annihilation of vacancies, which leads to suppressed growth of detrimental He bubbles (smaller diameter) in Ni-based CSAs subjected to irradiation. Similarly, Chen et al. have found that the average He bubble size in NiCoFeCr is smaller than that in Ni or steel under comparable irradiation conditions.[13] Chemical effects on He bubble superlattice formation in SP-CSAs have recently been investigated under 30 keV He implantation at room

temperature.[14] The size of He bubbles increased with increasing fluence, ranging from ~ 1×10^{17} cm^{-2} to 4×10^{17} cm^{-2} in Ni and CSAs as expected; but smaller bubbles—reduced by nearly 30%—formed in NiFe and NiCoFeCr under the same fluence, compared with those in the pure Ni metal. Moreover, the necessity of a higher fluence to form superlattices in CSAs is attributed to sluggish defect migration. Furthermore, Harrison et al.[14] have noted that, as alloy complexity is increased, the formation of He-vacancy clusters with a higher He/vacancy ratio in CSAs is possible for the same fluence of He ions.

Although it has long been observed that specific compositions in diluted and/or concentrated alloys have higher radiation or swelling resistance than their pure metal counterparts, the underlying defect mechanisms remain unclear. The studies of SP-CSAs suggest that local structural distortion and chemical disorder could impact cavity formation, calling attention to the heterogeneity at the level of electrons and atoms resulting from alloying certain elements together.[3] In this work, using SP-CSAs composed of 3*d* transition metals as model alloys, we investigate chemically-biased void swelling and He bubble formation. The work is described in two main parts, in the Result (Section 3) the experimental evidences of the electronic effects (i.e., 3*d* electron configurations with large differences in the outermost electron counts) on both void and He bubble formation; and in Discussion (Section 4) the underlying mechanisms (e.g., *d* electron effects on *heat conduction and dissipation*, *defect energetics*, and *sluggish diffusion and chemically-biased atomic transport*). We highlight the effects of 3*d* electrons on heat conduction and defect energetics, as well as on chemically-biased atomic transport, which are shown to affect cavity formation and evolution under both self-ion Ni irradiation and He implantation.

2. Material and experimental procedure

2.1. Crystal Growth

Single crystals of pure Ni and SP-CSAs—both in equiatomic concentrations (NiCo, NiFe, and NiCoFeCr) and in the form of non-equiatomic binary alloys of $Ni_xFe_{(1-x)}$ with x= 0.8, 0.65, and 0.5—were produced by arc melting and drop casting using high-purity elemental metals. They were subsequentially solidified to produce single crystals.[15] The crystalline rods were cut normal to the [100] directions and carefully polished to produce damage-free surfaces for irradiation experiments. Some physical properties[7,15,16] of the crystals are provided in Table 1. The Ni and all the alloys in this work were composed of 3*d* transition metals with a face-centered cubic (fcc) structure; they were chosen as model alloys because of their similarities, to highlight the chemical effects arising from differences in the outermost occupied shell. As shown in Table 1, the alloys had a slightly lower mass density than pure Ni as a result of alloying lighter masses. The lattice parameters and melting temperatures were similar, ranging from 3.524 to 3.583 Å and 1695 to 1728 K, respectively.

2.2. keV He implantation and MeV Ni ion irradiation

Nickel irradiations and He implantations for void swelling and He bubble formation were conducted at 500 °C (773 K), ~0.45 T_m (T_m is the melting temperatures, see Table 1). Irradiation-induced vacancies and injected He in the model systems were both expected to be mobile.

Implantations of 6 keV $^4He^+$ ions to a fluence of up to 6.1×10^{16} cm^{-2} with a flux of 3.4×10^{13} cm^{-2} s^{-1} were carried out using the Microscope and Ion Accelerator for Materials Investigation (MIAMI-1) facility, an in situ ion irradiation and transmission electron microscopy (TEM) system, at the University of Huddersfield.[17] Tilt implantations (7°) of 200 keV $^4He^+$ ions to fluences of 1×10^{16} and 5×10^{16} cm^{-2} with an average flux of 2×10^{13} $cm^{-2}s^{-1}$ were performed using the Danfysik Research Ion Implanter at the Ion Beam Materials Laboratory at Los Alamos National Laboratory (LANL). For the MIAMI-1 system,[17] the samples were heated using a Gatan 652 double tilt heating holder, and the He beam was 30° off the sample normal during the experiments. The ion implanter consists of a Colutron G-2 ion source capable of accelerating ions from 0.5 to 10 kV and a post-acceleration tube, allowing acceleration to 100 kV in total. For the 200 keV implantations at LANL, the heating rate was about 1 °C per 3 seconds for the ramp-up period, and the sample holder was subsequentially cooled naturally to room temperature after the implantation. During the implantations, the vacuum in the target chamber was kept at ~0.9×10^{-7} and 1.0×10^{-7} torr at Huddersfield and LANL, respectively

To evaluate void formation under displacement damage, self-ion irradiations were carried out using 1.5 MeV Ni^+ to fluences of 4×10^{14} and 3×10^{15} cm^{-2} and 3.0 MeV Ni^+ to 8×10^{16} cm^{-2}, respectively, at the Ion Beam Materials Laboratory at the University of Tennessee Knoxville.[18] Both Ni irradiations were performed at 7° off the surface normal, as was the case for the 200 keV He implantation, to avoid possible channeling effects along the (001) orientation. To ensure uniform irradiation, the Ni beam was defocused and wobbled in both the horizontal and vertical directions,[18] and the ion flux was ~ 1×10^{12} and 6.8×10^{12} $cm^{-2}s^{-1}$ for the 1.5 and 3.0 MeV Ni^+ irradiations, respectively.

2.3. Damage profile prediction

The Stopping and Range of Ions in Matter (SRIM) code, 2003 version,[19] both the full-cascade mode and the quick option, was used to estimate the displacement damage and ion concentration. In the SRIM calculations, a threshold displacement energy of 40 eV was assumed for all the constituent elements.[20] Recent studies[21,22] show that ion-induced damage in both monoatomic and multi-elemental targets with a significant mass difference should be predicted using the full-cascade simulations, as the quick Transport of Ions in Matter (TRIM) option based on Kinchin-Pease holds only for monoatomic targets.[23] To demonstrate the difference in the damage profile estimation, Fig. 1 shows SRIM predictions

in both full-cascade and quick modes of 6 keV He implantation in NiFe to an ion fluence of 6.0×10^{16} cm^{-2}. Significantly lower damage predictions from quick TRIM are evident. While the displacement damage estimated from the full-cascade mode is used for discussion, the SRIM predictions from both the full-cascade mode and the quick option are estimated for easy comparison or conversion.

Since the densities of pure Ni and of the alloys studied here are different (Table 1), the NiFe density of 8.2326 $g\cdot cm^{-3}$ (8.656×10^{22} $atoms\cdot cm^{-3}$) was used in the SRIM calculations to represent Ni and CSAs with densities varying from 8.1445 to 8.908 $g\cdot cm^{-3}$ (from 8.701×10^{22} to 9.14×10^{22} $atoms\cdot cm^{-3}$). SRIM predictions of implanted He or Ni ions in NiFe are shown in Figs. 1–3. Insignificant variance in SRIM predictions is expected from the differences in density. For example, the damage peak resulting from 1.5 MeV Ni irradiation in Ni or NiFe appears at ~385 or 400 nm, ~ 4% difference.

SRIM predictions of 6 keV 30° off surface normal He implantation are shown in Fig. 1. The ion distributions from both TRIM options are essentially the same with a peak He concentration of ~ 14% at 24 nm. The full width at half maximum (FWHM) ranged from 6 to 45 nm, suggesting that most of the implanted He remained in the TEM foils with a typical thickness of a few tens of nanometers. Much higher displacement damage was predicted from the full-cascade mode (Fig. 1a), ~ 1.89 times higher than that from quick TRIM. Although the shapes of the He-induced damage profiles were similar, a slightly deeper damage profile was predicted by full-cascade TRIM because of the forward momentum of recoils. For 200 keV He ions in NiFe, the conversion factor from ion fluence (10^{14} cm^{-2}) to peak damage in dpa, based on the full-cascade versus quick TRIM, is 0.0061 or 0.0024 at a depth of ~ 495 nm, respectively. The corresponding peak He concentration was 0.0055% at 545 nm.

For 1.5 and 3.0 MeV Ni irradiations, the simulations were done at 7° off the surface normal to be consistent with the irradiation. For an ion fluence of 10^{14} cm^{-2}, the peak concentration (0.0031%) of 1.5 MeV injected Ni was located at ~ 545 nm and the peak damage was located at ~ 400 nm. The conversion factors from ion fluence were 0.314 and 0.131, respectively, from the full-cascade and quick options. Similarly, for the 3.0 MeV Ni irradiation, the peak concentration (0.0021%) for an ion fluence of 10^{14} cm^{-2} was located at ~ 1160 nm and the peak damage was located at ~ 960 nm with a conversion factor of 0.258 from the full-cascade simulation.

2.4. TEM characterization

Post-TEM examinations were conducted at the University of Michigan[6,24] and at Oak Ridge National Laboratory (ORNL)[11,12] on Ni-irradiated and He-implanted samples, respectively; and in situ TEM characterization to monitor He bubble formation in Ni and in NiCoFeCr was carried out at the University of Huddersfield.[14,17] Focused-ion beam (FIB) lift-out techniques were used to prepare cross-

sectional TEM and scanning TEM (STEM) samples. Flash polishing[6] was used when necessary to remove damage from the gallium ion beam in the FIB.

All the cross-sectional TEM images were obtained at the University of Michigan using a JEOL 3100 operated at 300 kV under two-beam conditions with **g**=[200] for the 1.5 MeV Ni-irradiated samples (Fig. 2) and a JEOL JEM-2100F microscope on-zone [110] STEM for the 3.0 MeV irradiated samples (Fig. 3). The MIAMI-1 facility[17] was used to follow the microstructural evolution under 6 keV He implantation. The system consists of a JEOL JEM-2000FX operated at 200 kV, where the ion beam is 30° off the electron beam. (Further details for the MIAMI-1 facility can be found elsewhere.[17]) Post-TEM analyses at ORNL of He bubbles induced from 200 keV He implantation were conducted using a FEI Titan microscope operated at 300 kV. Bright field (BF)-TEM images were acquired at an under-focused condition, so that He bubbles appeared as light discs surrounded by a sharp dark fringe. In acquiring these BF-TEM images, the samples were tilted to higher-order zone axes to minimize the interference of contrast from dislocations. The size distribution of the He bubbles was obtained by statistical processing of more than 900 bubbles for each sample.

3. Results

Damage evolution under ion irradiation at elevated temperature is a series of complex nonequilibrium processes that involve many interconnected defect dynamics (e.g., vacancy and interstitial production, annihilation, diffusion, clustering, decomposition, segregation). Under high-temperature ion irradiation at ~ 0.45 T_m, both interstitials and vacancies are expected to be mobile. Moreover, because of the low formation energies for vacancies over interstitials,[25] thermally induced vacancies are anticipated. To uncover the effects of heterogeneity resulting from alloying 3*d* transition metals with different electron outermost shell occupation we, in a very simplified picture, focus the discussions on 3*d* electrons and chemically-biased mass transport through the dynamic evolution of interstitial- and vacancy-type defects. Five subsections are outlined to show the experimental evidences of the electronic effects. Section 3.1 is devoted to ion-irradiation induced void swelling in Ni and 3 model SP-CSAs (NiCo, NiFe and NiCoFeCr). This special set of Ni-based SP-CSAs composed of 3*d* transition metals represents different levels of chemical complexity, increased by the number of multiple principal elements (from 1 to 2 and to 4) or altered by replacing the principal elements (in the binaries of NiCo and NiFe by replacing Co with Fe). Four subsections are delineated to show the differences in He bubble formation resulting from the electronic effects. Bubble formation in Ni, NiCo and NiFe (i.e., $Ni_{0.5}Ni_{0.5}$, $Ni_{0.5}Co_{0.5}$ and $Ni_{0.5}Fe_{0.5}$) are described in Section 3.2 to show the impact of replacing 50% Ni in Ni with Co or Fe. Section 3.3 is devoted to show the effects of tunable chemical complexity on bubble formation that, by increasing the Fe concentration in $Ni_xFe_{(1-x)}$ with x = 1, 0.8, 0.65 and 0.5 (i.e., from Ni to $Ni_{0.8}Fe_{0.2}$, $Ni_{0.65}Fe_{0.35}$, and

$Ni_{0.5}Fe_{0.5}$), large bubbles are effectively suppressed with higher Fe concentration. Moreover, He bubble formation in Ni (lack of chemical complexity) and NiCoFeCr (chemically complex alloy) are studied both via *in situ* TEM observation (Section 3.4) and post-TEM characterization (Section 3.5) to further demonstrate strong effects of 3*d* electron configurations.

3.1 Void formation in Ni, NiCo, NiFe, and NiCoFeCr under Ni ion irradiation

Void formation under 1.5 MeV Ni^+ irradiation at ~0.45 T_m was characterized in Ni, NiCo, and NiFe (Fig. 2). The SRIM full-cascade model predicted damage profiles (indicated by long-dash lines) and injected Ni concentration (short-dash lines) for fluences of 4×10^{14} and 3×10^{15} cm^{-2} are overlaid on the corresponding NiFe samples (Figs. 2c and f), respectively. The grey bands in Fig. 2b result from insignificant bending of the NiCo sample. Although NiCo and NiFe are both fcc binaries, suppression of void formation is apparent in NiFe (Figs. 2c and f) but not in NiCo (Figs. 2b and e). While similar distributions of void formation are observed in Ni and NiCo (Figs. 2a, b, d and e), void formation is significantly delayed in NiFe.

As shown in the left column of Fig. 2, relatively larger voids are observed underneath the surface, ranging from 200 to 700 nm (average dose of ~1 dpa), in Ni and in NiCo under 4×10^{14} cm^{-2} with a peak dose of 1.26 dpa. Somewhat unexpected is the narrow band of low-density small voids observable in NiFe at the end of the ion range (from 700 to 850 nm, average dose below 0.1 dpa). As the fluence increases to 3×10^{15} cm^{-2} (Fig. 2 right column, peak damage 9.4 dpa), the voids clearly grow in both size and density over a wider depth, from 200 to 800 nm in Ni and from 200 to 1250 nm in NiCo. For NiFe, compared with the low-fluence sample (Fig. 2c), the voids, also grown in size (Fig. 2f), are more visible; and the band of the voids extends from 750 to 950 nm because of the higher-fluence irradiation.[6]

Inspection of Fig. 2 shows that the void distribution in Ni and NiCo is roughly consistent with the SRIM-predicted damage profile, which peaked at ~ 400 nm. Contrary to the findings in Ni and NiCo, the void bands in NiFe appear at the end of the ion range (e.g., ~ 850 nm, Fig 2c and f), much deeper than the void bands in Ni and NiCo. The results in Fig. 2 are similar to those in our previous work[6,24] showing that the relative locations of voids and interstitial loops are different in NiFe from those observed in Ni and NiCo. Upon irradiation to 4×10^{14} and 3×10^{15} cm^{-2}, voids in Ni and NiCo are distributed closer to the surface than dislocations,[6,24] while dislocations in NiFe are nearer the surface than voids.[24] These observed differences may be related to the strength of electronic deformation (the capability for charge transfer between neighboring atoms) and chemically-biased mass transport in NiFe, as discussed in Section 4.

To minimize the influence from the surface effect and to demonstrate the impact from concentration of the alloying element, radiation responses in Ni, $Ni_{0.8}Fe_{0.2}$ and $Ni_{0.5}Fe_{0.5}$ (NiFe) are investigated under irradiation with 3 MeV Ni^+ to 8×10^{16} cm^{-2}, much higher than the fluences used shown

in Fig. 2. Bright-field STEM (BF-STEM) images on-zone [110] are shown in Fig. 3 to reflect both voids and interstitial loops. Comparing the 3 MeV results (Fig. 3) with the 1.5 MeV results (Fig. 2), no apparent surface effects can be identified under either irradiation. The size of void in Ni (Fig. 3a) increases due to higher fluence, therefore, higher local dose, as comparing the overlaid SRIM results in Figs. 2c, 2f and 3c. For the 3 MeV Ni irradiation, the peak dose is over 200 dpa around damage peak region, from 860 to 1010 nm. Void suppression is evident in $Ni_{0.8}Fe_{0.2}$ and NiFe in the irradiated region. For the $Ni_{0.8}Fe_{0.2}$ sample (fig. 3b), although no voids are observed in the irradiated region up to 1400 nm, a few sizable voids are formed at the end of ion range at ~ 1500 nm and deeper. In the NiFe sample (Fig. 3c), higher densities of shorter dislocations and loops are observed, as compared with the Ni and $Ni_{0.8}Fe_{0.2}$ samples. Moreover, it is worth noting that void swelling is completely suppressed in NiFe at doses up to 200 dpa.

3.2 Bubble formation in Ni, NiCo and NiFe under He ion implantation

Helium bubble formation in pure Ni and in equiatomic binaries of NiCo and NiFe was investigated under irradiation using 200 keV He ions at 500 °C to a fluence of 5×10^{16} cm^{-2}. Similar to the void formation shown in Fig. 2, He cavity formation is somewhat comparable in Ni and NiCo but is clearly delayed in NiFe. Typical TEM images of He bubble distributions in implanted samples are shown in Fig. 4. While bubbles formed in all three crystals, those in Ni and NiCo had a wider size distribution with more relatively large bubbles (e.g., 10–12 nm in diameter), which were rarely observed in NiFe (in which bubbles were mainly ~ 6.5 nm in diameter). In particular, the bubble sizes exhibit a unique bimodal distribution in both Ni and NiCo: both large (e.g., >10 nm diameter) and small bubbles (e.g., <3 nm diameter) can be seen. Compared with Ni, it is evident that bubble growth is suppressed in NiFe but less so in NiCo. A similar observation was reported by Fan et al.[11] in Ni-based binary alloys of $Ni_{0.8}M_{0.2}$ where M was chromium (Cr), manganese (Mn), Fe, and cobalt (Co). Smaller bubble sizes are found in Ni alloyed with Cr and Mn than with Fe. Alloying with Co had a limited effect, as the largest bubble size was found in $Ni_{0.8}Co_{0.2}$ compared with the other $Ni_{0.8}M_{0.2}$ alloys. The trend of reduced bubble size ($Ni_{0.8}Co_{0.2}$ > $Ni_{0.8}Fe_{0.2}$ > $Ni_{0.8}Cr_{0.2}$ > $Ni_{0.8}Mn_{0.2}$) emphasizes the need to investigate the characteristics of the transition metal elements—differences in 3*d* electrons.

3.3 He Bubble formation in $Ni_xFe_{(1-x)}$ with x = 1, 0.8, 0.65 and 0.5

Since NiFe outperforms Ni and NiCo under both Ni and He bombardment, the concentration effect of alloying with Fe in the Ni-Fe binary alloys was investigated under 200 keV $^4He^+$ implantation using $Ni_xFe_{(1-x)}$, with x decreasing from 1 to 0.5. The resulting He bubbles and the corresponding size distribution are shown in Figs. 5 and 6, respectively. The analysis of size distribution (Fig. 6) was performed based on multiple images, as shown in Fig. 4, taken at a depth between 100 nm and 350 nm.

This region, 100 nm from the surface and ~200 nm shallower than the peak He concentration (shown in Fig. 4), was chosen to minimize the influence of both the surface and the injected He (<0.5%). Clearly, with increasing Fe concentration, the cavity size decreases, similar to the observation of void suppression under Ni irradiation shown in Fig. 3. Large bubbles are significantly suppressed with Fe concentrations of 35 and 50% (Figs. 6c and d). As is discussed later in Section 4.3, the observed concentration dependence was attributed to percolation effects and chemically-biased mass transport in NiFe binary systems.

3.4 In situ TEM observation of He bubble formation in Ni and NiCoFeCr

Not limited to binary systems, formation of He bubbles in Ni and NiCoFeCr was monitored under 6 keV He^+ ion implantation at 500°C using MIAMI-1. The evolution under three similar fluences is shown in Figs. 7 and 8 for comparison. Helium bubbles started to form in Ni at fluences of 2.73×10^{16} cm^{-2}, just before the images shown in Figs. 7a and d (2.75×10^{16} cm^{-2}). A slightly higher fluence was needed for bubble formation in NiCoFeCr. No bubbles are observed in NiCoFeCr at 2.73×10^{16} cm^{-2} (Figs. 8a and d), but they are clearly observable at fluences of 3.77×10^{16} cm^{-2} and 6.1×10^{16} cm^{-2} (Figs. 8b/e and c/f) as shown by the contrast in under/overfocus conditions, respectively. Besides the higher fluence needed to form bubbles in NiCoFeCr, the bubbles developed more quickly and were larger in Ni than in NiCoFeCr. Bubble sizes at the end of the He implantation in Ni and NiCoFeCr are compared using higher-magnification images in Fig. 9. Larger bubbles are observed in Ni, whereas the bubble size is mostly ~1 nm in NiCoFeCr.

3.5 Post-TEM characterization of He bubble formation in Ni and NiCoFeCr

To compare He depth distribution, He bubble formation was investigated under 200 keV He implantation to 1×10^{16} cm^{-2} in Ni and NiCoFeCr (Fig. 10). With a peak He concentration of ~0.5 %, bubbles are easily seen in both samples. Similar to the higher-fluence Ni sample shown in Fig. 4a, a bimodal distribution has already developed at this fluence (Fig. 10a), with coexisting large and small bubbles. The grey bands in Fig. 10a are bend contours resulting from a small degree of bending of the sample. A moderately narrower size distribution is noticeable in NiCoFeCr (Fig. 10b), and bubbles are located in a region with a relatively high He concentration (>0.1%, from ~350 to 660 nm, as shown by two vertical dotted lines). Compared with NiCoFeCr, a wider bubble distribution is observed in Ni: significantly more bubbles appear deeper into the sample and close to the surface. Statistical analysis of the bubble sizes is performed from more than 700 bubbles in each sample. The investigated region is between 50 nm to 400 nm below the surface, as in the analysis done in Fig. 6. Bubble number volume density in Ni and NiCoCrFe is 1.89×10^{-5} and 1.67×10^{-5} nm^{-3}, respectively.

4. Discussion

Many SP-CSAs with an fcc structure consist of 3*d* transition metals, namely Cr ($3d^5 4s^1$), Mn ($3d^5 4s^2$), Fe ($3d^6 4s^2$), Co ($3d^7 4s^2$), and Ni ($3d^8 4s^2$),. Section 3 discusses experimental studies carried out in Ni and a few model SP-CSAs to understand the formation of void and He cavities under Ni self-ion irradiation and He implantation. The systems in this work were chosen with the aim of limiting variables that could affect the observed difference in radiation responses. Specifically, pure Ni, NiCo, $Ni_xFe_{(1-x)}$, and NiCoFeCr are composed of 3*d* transition metals, all in an fcc structure. As shown in Table 1, Ni and the CSAs have similar mass, density, lattice parameters, and melting temperature. While cavity formation and evolution under ion irradiation at elevated temperature are complex processes, in a very simplified picture using Ni and the model alloys, our aim was to highlight the chemical effects resulting from the alloying of 3*d* transition metals with different electron band occupations (orbital configurations).

In the periodic table, elements in different groups or subgroups (with different electron counts, or differences in the number of electrons in the conduction and valence bands) generally have dissimilar chemical behavior and properties. For period-4 3*d* transition metals, the highest electron configurations (outermost electrons) of transition metal atoms are in a 3*d* sub-shell, as well as in the hybridized 4*s* and 3*d* orbitals. The electrons sequentially fill their 4*s* shells first, then their 3*d* shells, except for Cr (6 electrons, the maximum number of unpaired electrons for a *d*-subshell) and copper (11 electrons, near the end of the transition series in which $3d^{10}4s^1$ is more stable than $3d^9 4s^2$). The random lattice site occupancy of different period-4 metals creates significant disorder in the electronic structures of the alloys,[5,7,26,] although the disorder is often less significant in the lattice distortion because of the similar atomic size.[27-31] The chemical complexity in SP-CSAs made of 3*d* transition metals has been shown to provide a way to modify paths for energy dissipation and defect evolution.[3-7] For example, the physical origin of a two-orders-of-magnitude resistivity difference is demonstrated in alloys containing combinations of the closely related elements Ni, Co, Fe, Mn, and Cr.[7,16] The electronic transport and the energy dissipation in random alloys can be modified by choosing the number and the types of alloying elements.[26] In addition to the substantial reduction in electrical and thermal conductivity, increasing chemical disorder also leads to substantially modified defect formation energies and migration barriers;[25,32] consequently, defect production and microstructural evolution are notably affected.[3-7,27] In the following discussion, we focus on compositional complexity (resulting from ***d* electron effects**) that leads to differences in *heat conduction and dissipation*, *defect energetics,* and *mass transport* that consequently affect defect dynamics at the early stage of radiation damage and ultimately reduce the surviving defects and enhance radiation tolerance.

4.1 Effects of 3*d* electrons on heat conduction and dissipation

The outermost electrons in an atom are the ones involved in chemical bonding and electrical conductivity, and the formation of the electronic band structure is attributed to the outermost electrons. The mean free path, intrinsic to a material's electronic band structure, maps electrical propagation in the material, which reflects how good electrons are at conducting electricity and heat. Specifically, in a perfect crystal lattice such as in pure Ni, energy dissipates quickly by its electrons due to little scattering—an infinite mean free path (i.e., high κ and low ρ, especially at 5 and 50 K, for Ni in Table 1). In SP-CSAs alloys of NiCo, NiFe and NiCoFeCr, transport measurements[7,16] show that increasing the number of alloying elements with large differences in *d* electron counts can create more substantial chemical disorder, which leads to a much reduced mean free path and significantly reduces electrical and thermal conductivity (low κ and high ρ for the alloys in Table 1) and results in inefficient heat conduction. Calculations demonstrate that electrical conductivity is modified as a result of the broadening of the electronic band structure by chemical disorder.[7,26] Research shows that electrical resistivity arises from spin-dependent (majority-spin, minority-spin) electron scattering. For alloys containing only Co and Ni, the majority-spin channel experiences negligible electron scattering, thereby providing low electrical resistivity; for Cr- and Mn-containing alloys, in contrast, strong electron scattering occurs in both spin channels, leading to high electrical resistivity. We note the partially filled *d* bands of Cr and Mn versus the nearly full *d* bands of Co and Ni in these studies;[7,26]; they suggest that alloy properties may be manipulated to technological advantage through the number and types of alloying elements and, more explicitly, the difference in the 3*d* electron counts.

Nonadiabatic energy transfer between atoms and electrons is controlled by the strength of the electron-phonon (*el-ph*) coupling as one of the intrinsic properties of specific alloys.[33-35] Dissipation of inelastic energy (deposited to electrons) interacts with elastic energy transfer processes (energy deposited simultaneously to atomic recoils), which influences the shape and size of collision cascade damage. The substantial reduction of electrical and thermal conductivities in SP-CSAs highlights the need to pay attention to the local heat dissipation.

While pure Ni metal has a long mean free path and is a good conductor of electricity and dissipater of heat—properties that are desirable for some applications—some SP-CSAs with dramatically reduced ability to conduct electron energy and dissipate heat (such as NiFe and NiCoFeCr) can offer significant improvement in resistance to radiation damage.[3,5,6] The more profound the chemical complexity, the smaller the defect clusters produced,[4,24] which is beneficial to materials performance in harsh nuclear applications. Since implanted He atoms are expected to bind closely with vacancies, the modified defect dynamics in SP-CSAs due to the *d* electron effects on heat conduction and dissipation is also anticipated to impact He cavity evolution.

4.2 Effects of 3*d* electrons on defect energetics

Fundamental knowledge of the distribution of defect energetics, such as formation and migration energies, is indispensable for understanding the roles that different alloying elements play in radiation performance (e.g., diffusion paths, microscopic evolution under ion irradiation). Researchers have demonstrated that defect properties in CSAs composed of 3*d* transition metals are determined by their *d* electron characteristics.[36] In SP-CSAs, atomic-level variation in the alloying elements has a large influence on defect formation and migration energies.[25,37] Since each atom may experience a different local environment, the formation and migration energies of vacancies and interstitials exhibit a distribution rather than a single value as in a pure metal. While most vacancy formation energies in SP-CSAs are larger than those in Ni, the formation energies of [100] dumbbell interstitials are smaller than those in Ni. In general, migration energies of vacancies and interstitials exhibit a region of overlap, e.g., they are more significant for NiFe[25,38] (compared with NiCo) and for NiCoFeCr[36] (compared with NiCoCr). Considerable overlapping is an indication of enhanced defect annihilation.[25,36]

Explicitly, in NiCo,[38] the formation energies of Ni and Co vacancies are very similar, while the formation energies for Co–Co and Co–Ni dumbbell interstitials are lower than for Ni–Ni interstitials. In NiFe,[38] lower formation energies are found predominantly for Ni–Ni and Ni–Fe dumbbell interstitials and for Fe vacancies (rather than for Ni vacancies). Defect formation and migration energies in equiatomic NiCoCr and NiCoFeCr CSAs have been characterized using density functional theory (DFT).[36] Interestingly, distributions of migration energies for Cr/Fe interstitials and Cr/Fe vacancies are known to exhibit large overlap regions.[36] Analysis of their electronic structures reveals that the electronic deformation capability resulting from partially filled *d* electrons plays a critical role in governing defect migration energies.

For the model SP-CSAs in this work, the electronic densities of state, dominated by 3*d* electrons, can be further decomposed into $t_{2g}(\sigma)$ and $e_g(\pi)$ components. Recent modeling work[36] has revealed that the more significant the changes in the *d*-electron occupation in the t_{2g} and e_g orbitals for each alloying element (charge redistribution or transfer), the wider the distribution of migration barriers. Comparing the partially filled *d* electrons in Cr and Fe (Cr [$3d^5 4s^1$] and Fe [$3d^6 4s^2$]) with the late 3*d* transition elements in Co and Ni (Co [$3d^7 4s^2$] and Ni [$3d^8 4s^2$]), the electron densities of Fe/Cr elements are more flexible in accommodating defects. The charge redistribution is particularly noteworthy for the partially filled $t_{2g}(\sigma)$ band that points directly to the nearest neighbors, whereas the nearly full $e_g(\pi)$ band shows little charge transfer. For example, defect-free Cr atoms in NiCoCr have dominant t_{2g} states, shown as a diagonal elongation of the electronic density pointing to the nearest neighbors (with respect to the orthogonal simulation box). Introducing a Cr interstitial leads to a transition to e_g states (along the axial directions).[36] The partially filled *d* shells of Cr/Fe may provide additional deformation flexibility for electrons to

transfer from the t_{2g} to e_g states and make the migration of corresponding defects easier.[32,36] On the other hand, charge transfer is smaller for Ni because of its nearly full *d* band, so the electron density around Ni atoms is rigid and difficult to deform. Similarly, the charge redistribution is also small for Co, for which the *d* band is more than 80% full.[36] The relationship between the changes in electron orbital occupation and the barrier heights reveals the impact of the *d* electrons on defect properties. In addition, modeling work[36-38] indicates that interactions between interstitials and vacancies are enhanced in alloys with alloying elements that have large differences in 3*d* electron counts, leading to enhanced defect recombination.

Based on the modeling work discussed above,[36-38] one can hypothesize that the electronic deformation capability of Cr/Mn/Fe with half-filled electron band structures is high compared with that of Ni/Co/Cu. The deformation capability has a dominant effect on the migration energies of the different elements in SP-CSAs. The partially filled *d* electron orbitals and their flexible electron densities make it easy to accommodate defects and thus should result in a beneficially wide distribution of their migration energies. One may further expect a narrower gap between the migration energies of interstitials and vacancies to promote interstitial-vacancy recombination, leaving fewer available vacancies to contribute to He bubble growth. Such an assumption was proved recently.[11,12] Combined TEM experiments and DFT calculations on five Ni-based alloys ($Ni_{0.8}X_{0.2}$, X = Co, Fe, Cr, Pd, Mn) have shown that $Ni_{0.8}Mn_{0.2}$ has the smallest difference in vacancy-interstitial migration energies and the least radiation damage accumulation (e.g., the smallest cavities).

4.3 Sluggish diffusion and chemically-biased atomic transport

Local lattice distortions from the random arrangement of different chemical elements may be limited in SP-CSAs composed of 3*d* transition metals,[27,29,31] but defects are shown to experience a complex energy landscape.[3] Complex energy landscapes modify transport properties and defect behavior. The broken energy landscapes, that is, the absence of continuous low-energy diffusion trajectories, lead to sluggish diffusion and chemically-biased mass transport that may suppress damage growth and delay deleterious microstructural degradation, which may substantially improve radiation resistance.[8,9]

The effects of elementally biased defect transport have been revealed by molecular dynamics (MD) simulations showing slow 3D short-range diffusion of small interstitial clusters in NiFe, in contrast to 1D long-range migration in pure Ni and NiCo.[6,39-41] In contrast to a periodic energy landscape in pure metals, the landscape in concentrated alloys is highly distorted by local "traps".[41] Because of atomic-level chemical fluctuations, temporal traps are formed in which defect formation energies are low (i.e., mobile defects spend most of their time in these traps). Interactions among these traps depend on the alloy composition and the transport mechanisms that are activated (vacancies, interstitial atoms, defect clusters).

Classical MD modeling[40] has shown that the diffusion coefficients of small vacancy clusters in CSAs are higher than in pure Ni, but that they become much lower in large vacancy clusters. This observation suggests that large clusters can easily migrate in pure Ni and grow larger. In contrast, cluster growth is suppressed in many CSAs as a result of the limited mobility of large vacancy clusters. Moreover, the less frequent the interaction among these traps, the slower is the whole evolution process (property degradation is delayed or suppressed). One piece of evidence supporting slow migration in CSAs is found in a recent work on He superlattice formation after room-temperature 30 keV He implantation in Ni, NiFe, and NiCoFeCr.[14] Harrison et al. show that the He fluence required to make bubble ordering increased from ~8.0×10^{16} cm^{-2} in pure Ni, and ~9×10^{16} cm^{-2} in NiFe, to ~1.1×10^{17} cm^{-2} in NiCoFeCr. Moreover, smaller superlattice parameters and smaller bubble diameters were observed in NiFe and NiCoFeCr than in Ni. These phenomena were attributed to sluggish diffusion[14] that is closely related to chemically-biased mass transport.

It is worth noting that CSAs are unique materials in which percolation effects can be enhanced significantly by local chemistry to define material properties. To better understand chemically-biased diffusion, migration pathways of both interstitials and vacancies in model $Ni_xFe_{(1-x)}$ alloys have been modeled from the nanoscale to the mesoscale.[10,40-42] The results showed that percolation combined with local chemistry strongly affected vacancy diffusion and atomic transport and controlled the way in which local defect properties were integrated into the global behavior of defects. Based on multispatial/multitemporal atomistic simulation techniques—including DFT, microsecond-scale MD (μs-MD), on-the-fly kinetic Monte Carlo (kMC), and conventional kMC—a consistent picture emerged in which interstitial and vacancy diffusivities were composition dependent. For vacancy migration, a pronounced minimum tracer diffusion coefficient that was evidence of a sluggish diffusion phenomenon was found around the fcc lattice site percolation threshold at 20% Fe (i.e., each Fe atom had at least one Fe atom among its nearest neighbors). Because of chemically-biased diffusion, vacancies preferred to migrate within the Fe subsystem (i.e., a vacancy exchanged locations with a nearby Fe), and Fe-vacancy transport coefficients were found to be negative, predicting that vacancy sinks should be depleted with Fe.[10,41] Sluggish and chemically-biased diffusion for interstitial atom migration, and positive Ni-interstitial atom transport coefficients, were demonstrated by ab initio and classical MD, k-ART, and kMC modeling in the equiatomic Ni-Fe alloy.[38,39] Thus, atomic-scale modeling and theory unambiguously predict that, under irradiation, interstitial atoms drag Ni atoms along their diffusion paths, while the vacancy flux provides Fe atom transport in the opposite direction. These mechanisms lead to a segregation bias in interactions among mobile defects (vacancies, interstitial atoms, and their clusters) and defect sinks (e.g., dislocation loops, voids, He bubbles).[10] This theoretically predicted behavior provides the underlying physics to support recently revealed experimental results for radiation-induced segregation

in SP-CSAs.[43,44] In this work, the percolation effects are well reflected in the observations in Figs. 3, 5 and 6 that the formation and growth of both voids and He bubbles are suppressed and follow the trend from pure Ni to $Ni_{0.8}Fe_{0.2}$ to $Ni_{0.65}Fe_{0.35}$ and NiFe.

4.4 Void swelling and He bubble formation

Systematic understanding of the nonequilibrium evolution of void swelling and He bubble formation requires systematic study over a wide range of irradiation conditions, beyond the scope of the current work. Nonetheless, the effects of 3*d* electrons on *heat conduction and dissipation*, *defect energetics,* and *mass transport*, as well as the resulting impact on microstructural evolution, are clearly control factors.

The *d* electron effects are clearly shown in Figs. 2–6. Nickel irradiation-induced voids are much smaller in NiFe, (Fig. 2), which is mainly attributed to the reduction of electrical and thermal conductivity[7,16,] and to substantially modified defect formation energies and migration barriers.[25] Larger overlaps of the migration energies of vacancies and interstitials in NiFe led to enhanced defect annealing compared with Ni and NiCo. The effects are also shown as voids appearing at a much deeper depth in NiFe because of the lower formation energies for Fe vacancies (compared with Ni vacancies) and because, as a result of strong chemically-biased mass transport, vacancies prefer to migrate within the Fe subsystem. An understanding of percolation and chemically-biased mass transport provides insights into the way in which local properties in alloys are integrated into the global bulk properties. It is desirable to provide the minimum diffusion interactions between different local minimum energy configurations of rapidly migrating defects. Interactions between "localized chemical fluctuations or inhomogeneities" are minimized near the percolation threshold. The percolation thresholds are expected to be different for interstitials and vacancies.[10,41] For example, in the Ni-Fe system, the *ab initio* and classical MD studies demonstrate[38,41,42] that Ni atoms are the slowest species via the vacancy and the fastest via the interstitial mechanisms of diffusion. The modeling work[38,41,42] further reveals that vacancies have preference to migrate via Fe atoms and interstitials via Ni atoms. The thresholds for vacancy or interstitial migration are at 20% or ~50–65 at. % Fe concentration, respectively, depending on the simulation temperature. The percolation effects are shown in Figs. 3, 5 and 6. The alloying effect on defects was more significant in concentrated binary alloys ($Ni_{0.65}Fe_{0.35}$ and NiFe) than in more dilute binary alloys (Ni and $Ni_{0.8}Fe_{0.2}$) because of the concentration difference of alloying atoms and the interstitial dominant migration mechanisms in the irradiated region. Smaller cavities are desirable consequences of the loss of translational invariance associated with intrinsic chemical disorder.

Percolation and sluggish diffusion effects are closely related to chemically-biased diffusion, which leads to segregation bias, as mentioned previously. Segregation bias, in turn, provides a specific

mechanism of void healing under irradiation that contributes to suppressed void swelling in some concentrated alloys.[10,41] Supporting evidence can be found in the literature[8] that much smaller void sizes and less swelling are found in $Ni_{0.8}Cr_{0.2}$, $Ni_{0.8}Mn_{0.2}$, and $Ni_{0.8}Fe_{0.2}$ than in Ni under the same irradiation conditions. Comparing the three binaries,[8] the highest swelling and relatively larger void diameter have been observed in $Ni_{0.8}Fe_{0.2,}$ as compared with $Ni_{0.8}Cr_{0.2,}$ and $Ni_{0.8}Mn_{0.2,}$. Recent work has provided insight into void growth in irradiated Ni-Fe alloys from the viewpoint of chemically-biased diffusion.[10] Work based on combined experimental, theoretical, and modeling studies has revealed and delineated controlling mechanisms of improved swelling resistance observed in ion-irradiated Ni-Fe equiatomic alloys. The element-specific and composition-dependent features of atomic mass transport clearly show that chemically-biased diffusion via vacancies and interstitials causes segregations near defect sinks that lead to increasing segregation bias, which prevents void growth and converts void nuclei into Ni-rich precipitates. Nevertheless, complete suppression of the 1D glide of interstitial clusters/dislocation loops prevents production bias, increases sink strength, enhances the flow of Ni atoms toward interstitial components, and creates Fe-rich channels for vacancy migration out of the damage region (i.e., observed at the end of the range, strictly different from the Ni and NiCo shown in Fig. 2).

The effects of chemical complexity can substantially modify energy transport and dissipation under ion energy deposition, depending on the coupling strength of the local interactions. The modification can either be direct, through changes in the mean free path, or indirect, through changes in the flow of energy from electronic subsystem to the atomic subsystem via electron–phonon coupling.[33-35] Clearly, varying the chemical complexity of SP–CSAs has the potential to tune the mean free path, interaction strength, and energy dissipation. Consequently, such electronic and atomic-level chemical modification affects void and bubble formation, as well as the subsequent evolution. Although significant differences were observed in Ni and the binaries, the moderate structural modification in NiCoFeCr (Figs. 7–10) suggests that the careful choice of 3*d* transition metals with different electron counts may have a more noteworthy impact than the use of a greater number of principal alloying elements.

5. Conclusion

It was found that altering alloying, recipes to modify chemical disorder, can control the way in which energy dissipates and defects evolve in advanced alloys that contain significant amounts of multiple elements. In this work, we called attention to the underlying *d* electron effects and discussed the resulting *heat conduction and dissipation*, *defect energetics,* and *mass transport* in He bubble formation and void swelling. We have shown that alloying elements with large differences in *d* electron counts (i.e., via the selection of elements and their concentrations) can create more substantial chemical disorder (i.e., increasing chemical complexity) in SP-CSAs of 3*d* transition metals, which leads to suppression of He

bubble formation and cavity growth during irradiation. This finding may pave the way for designing new radiation-resistant structural materials for energy applications.

Acknowledgments

This work was supported as part of the Energy Dissipation to Defect Evolution (EDDE), an Energy Frontier Research Center funded by the U.S. Department of Energy, Office of Science, Basic Energy Sciences, under contract number DE-AC05-00OR22725. Electron microscopy analyses were performed as part of a user proposal at ORNL's Center for Nanophase Materials Sciences (CNMS), which is a DOE Office of Science User Facility. Helium implantations were supported by the Center for Integrated Nanotechnologies (CINT), a DOE Office of Science User Facility jointly operated by the Los Alamos and Sandia national laboratories. B.C.S. was supported by the Department of Energy, Office of Science, Basic Energy Sciences, Materials Sciences and Engineering Division. The MIAMI-1 system at Huddersfield was funded by the UK Engineering and Physical Sciences Research Council (EPSRC) under grant number EP/E017266/1.

References

1. H. Trinkaus, B. Singh, Helium accumulation in metals during irradiation - where do we stand? J. Nucl. Mater. 323 (2003) 229–242.
2. B. Gludovatz, A. Hohenwarter, D. Catoor, E.H. Chang, E.P. George, R.O. Ritchie, A fracture-resistant high-entropy alloy for cryogenic applications. Science, 345 (2014) 1153–1158.
3. Y. Zhang, S. Zhao, W.J. Weber, K. Nordlund, F. Granberg and F. Djurabekova, Atomic-level heterogeneity and defect dynamics in concentrated solid-solution alloys, Curr. Opin. Solid State Mater. Sci. 21 (2017) 221–237.
4. F. Granberg, K. Nordlund, M.W. Ullah, K. Jin, C. Lu, H. Bei, L.M. Wang, F. Djurabekova, W.J. Weber, Y. Zhang, Mechanism of radiation damage reduction in equiatomic multicomponent single phase alloys, Phys. Rev. Lett. 116 (2016) 135504
5. Y. Zhang, K. Jin. H. Xue, C. Lu, R.J. Olsen, L.K. Beland,. M.W Ullah, S. Zhao, H. Bei, D.S. Aidhy, G.D. Samolyuk, L. Wang, M. Caro, A. Caro, G.M. Stocks, B.C. Larson, I.M. Robertson, A.A. Correa, W.J. Weber, Influence of Chemical Disorder on Energy Dissipation and Defect Evolution in Advanced Alloys, J. Mater. Res. 31 (2016) 2363–2375.
6. C. Lu, L. Niu, N. Chen, K. Jin, T. Yang, P. Xiu, Y. Zhang, F. Gao, H. Bei, S. Shi, M. He, I.M. Robertson, W.J. Weber, and L. Wang, Enhancing radiation tolerance by controlling defect mobility and migration pathways in multicomponent single-phase alloys, Nat. Commun. 7 (2016) 13564.
7. Y. Zhang, G.M. Stocks, K. Jin, C. Lu, H. Bei, B.C. Sales, L. Wang, L.K. Béland, R.E. Stoller, G.D. Samolyuk, M. Caro, A. Caro, W.J. Weber, Influence of chemical disorder on energy dissipation and defect evolution in concentrated solid solution alloys, Nat. Commun. 6 (2015) 8736.
8. T. Yang, C. Lu, G. Velisa, K. Jin, P. Xiu, M. Crespillo, Y. Zhang, H. Bei, L. Wang, Effect of alloying elements on defect evolution in Ni-20X binary alloys, Acta Mater. 151 (2018)159–168.
9. T. Yang, C. Li, S. J. Zinkle, S. Zhao, H. Bei, and Y. Zhang, Irradiation responses and defect behavior of single-phase concentrated solid solution alloys, J. Mater. Res. 33 (2018)3077–3091.

10. A. Barashev, Y.N. Osetsky, H. Bei, C. Lu, L. Wang, Y. Zhang, Chemically-Biased Diffusion and Solute Segregation Impedes Void Growth in Irradiated Ni-Fe Alloys, Curr. Opin. Solid State Mater. Sci. 23 (2019) 92–100.
11. Z. Fan, S. Zhao, K. Jin, D. Chen, Y. Osetskiy, Y. Wang, H. Bei, K. More, Y. Zhang, Helium irradiated cavity formation and defect energetics in Ni-based binary single-phase concentrated solid solution alloys, Acta Mater. 164 (2019)283–292.
12. X. Wang, K. Jin, D. Chen, H. Bei, Y. Wang, W. J. Weber, Y. Zhang, K. L. More, Effects of Fe concentration on helium bubble formation in NiFex single-phase concentrated solid solutions alloys, Materialia 5 (2019) 100183.
13. D. Chen, Y. Tong, H. Li, J. Wang, Y.L. Zhao, A. Hu, J.J. Kai, Helium accumulation and bubble formation in FeCoNiCr alloy under high fluence He^+ implantation, J. Nucl. Mater. 501 (2018) 208–216.
14. R.W. Harrison, G. Greaves, H. Le, H. Bei, Y. Zhang, S.E. Donnelly, Chemical effects on He bubble superlattice formation in high entropy alloys, Curr. Opin. Solid State Mater. Sci. (2019).
15. Z. Wu, H. Bei, F. Otto, G.M. Pharr, E.P. George, Recovery, recrystallization, grain growth and phase stability of a family of FCC-structured multi-component equiatomic solid solution alloys. Intermetallics 46, (2014) 131–140.
16. K. Jin, B.C. Sales, G.M. Stocks, G.D. Samolyuk, M. Daene, W.J. Weber, Y. Zhang, H. Bei, Tailoring the physical properties of Ni-containing single-phase equiatomic alloys by modifying the chemical complexity, Scientific Reports 6 (2016) 20159.
17. J.A. Hinks, J.A. van den Berg, S.E. Donnelly, MIAMI: Microscope and ion accelerator for materials investigations, J. Vac. Sci. Technol. A Vacuum, Surfaces, Film. 29. (2011) 21003,.
18. Y. Zhang, M.L. Crespillo, H. Xue, K. Jin, C.H. Chen, C.L. Fontana, J.T. Graham, W.J. Weber, New ion beam materials laboratory for materials modification and irradiation effects research, Nucl. Instrum. Methods Phys. Res. B 338 (2014) 19–30.
19. J.F. Ziegler, M.D. Ziegler, J.P. Biersack, SRIM – The stopping and range of ions in matter, Nucl. Instrum. Methods Phys. Res. B 268 (2010) 1818–1823.
20. ASTM E521, Standard Practice for Neutron Radiation Damage Simulation by Charged-Particle Irradiation, Annual Book of ASTM Standards, Vol. 12.02, ASTM International, West Conshohocken, PA, 2009
21. J.-P. Crocombette, C. Van Wambeke, Quick calculation of damage for ion irradiation: implementation in Iradina and comparisons to SRIM, EPJ Nucl. Sci. Tech. 5 (2019) 7 1-9.
22. W.J. Weber, Y. Zhang, Predicting Damage Production in Monoatomic and Multi-elemental Targets using Stopping and Range of Ions in Matter Code: Challenges and Recommendations, Curr. Opin. Solid State Mater. Sci. (2019).
23. N. Andersen, P. Sigmund, K. Dan, Vidensk. Selsk. Mat.-Fys. Medd. 39 (1974) 1–45.
24. C. Lu, K. Jin, L.K. Beland, F. Zhang, T.-ni Yang, L. Qiao, Y. Zhang, H. Bei, H.M. Christen, R.E. Stoller, L. Wang, Direct Observation of Defect Range and Evolution in Ion-Irradiated Single Crystalline Ni and Ni Binary Alloys, Scientific Reports 6 (2016) 19994.
25. S. Zhao, G.M. Stocks, Y. Zhang, Defect energetics of concentrated solid-solution alloys from ab initio calculations: $Ni_{0.5}Co_{0.5}$, $Ni_{0.5}Fe_{0.5}$, $Ni_{0.8}Fe_{0.2}$ and $Ni_{0.8}Cr_{0.2}$, Phys. Chem. Chem. Phys. 18 (2016) 24043.
26. S. Mu, G.D. Samolyuk, S. Wimmer, M.C. Troparevsky, S. Khan, S. Mankovsky, H. Ebert, G.M. Stocks, Uncovering electron scattering mechanisms in NiFeCoCrMn derived concentrated solid solution and high entropy alloys, npj. Computational Materials 5, (2019) 1.
27. H.S. Oh, S.J. Kim, K. Odbadrakh, W.H. Ryu, K.N. Yoon, S. Mu, F. Körmann, Y. Ikeda, C.C. Tasan, D. Raabe, T. Egami, E.S. Park, Engineering atomic-level complexity in high-entropy and complex concentrated alloys, Nat. Commun. 10 (2019) 2090.

28. F.X. Zhang, S. Zhao, K. Jin, H. Xue, G. Velisa, H. Bei, R. Huang, J.Y. P. Ko, D.C. Pagan, J.C. Neuefeind, W.J. Weber, Y. Zhang, Local structure and short-range order in a NiCoCr solid solution alloy, Phys. Rev. Lett. 118 (2017) 205501.
29. F.X. Zhang, Y. Tong, K. Jin, H. Bei, W.J. Weber, A. Huq, T. Lanzirott, M. Newville, D.C. Pagan, J. Y. P. Ko, Y. Zhang, Chemical complexity induced local structure distortion in NiCoFeMnCr high entropy alloy, Mater. Res. Lett. 6 (2018) 450–455.
30. Y. Tong, G. Velisa, S. Zhao, W. Guo, T. Yang, K. Jin, C. Lu, H. Bei, J. Y. P. Ko, D. C. Pagan, Y. Zhang, L. Wang, F. X. Zhang, Evolution of local lattice distortion under irradiation in medium- and high-entropy alloys, Mater. 2, (2018) 73–81.
31. Y. Tong, K. Jin, H. Bei, J. Y. P. Ko, D. C. Pagan, Y. Zhang, F. X. Zhang, Local lattice distortion in NiCoCr, FeCoNiCr and FeCoNiCrMn concentrated alloys investigated by synchrotron X-ray diffraction, Mater. Des. 155 (2018) 1–7.
32. D.B. Miracle, O.N. Senkov, A critical review of high entropy alloys and related concepts, Acta Mater. 122, (2017) 448–511.
33. A.A. Leino, G.D. Samolyuk, R. Sachan, F. Granberg, W.J. Weber, H. Bei, J. Lie, P. Zhai, Y. Zhang, GeV ion irradiation of NiFe and NiCo: Insights from MD simulations and experiments, Acta Mater. 151 (2018)191–200.
34. R. Sachan, M.W. Ullah, M.F. Chisholm, J. Liu, P. Zhai, D. Schauries, P. Kluth, C. Trautman, H. Bei, W.J. Weber, Y. Zhang, Radiation-induced extreme elastic and inelastic interactions in concentrated solid solutions, Mater. Des. 150 (2018) 1–8.
35. N. Sellami, A. Debelle, M.W. Ullah, H.M. Christen, J. K. Keum, H. Bei, H. Xue, W.J. Weber, Y. Zhang, Effect of electronic energy dissipation on strain relaxation in irradiated concentrated solid solution alloys, Curr. Opin. Solid State Mater. Sci. 23 (2019) 107–115.
36. S. Zhao, T. Egami, G.M. Stocks, Y. Zhang, Effect of *d* electrons on defect properties in equiatomic NiCoCr and NiCoFeCr concentrated solid solution alloys, Phys. Rev. Mater. 2 (2017) 013602.
37. S. Zhao, W.J. Weber, Y. Zhang, Unique Challenges for Modeling Defect Dynamics in Concentrated Solid-Solution Alloys, JOM 69 (2017) 2084–2091.
38. S. Zhao, Y.N. Osetsky, Y. Zhang, Preferential diffusion in concentrated solid solution alloys: NiFe, NiCo and NiCoCr, Acta Mater. 128, (2017) 391–399.
39. L.K. Béland, Y.N. Osetsky, R.E. Stoller, The effect of alloying nickel with iron on the supersonic ballistic stage of high energy displacement cascades, Acta Mater. 116 (2016) 136–142.
40. S. Zhao, G. Velisa, H. Xue, H. Bei, W.J. Weber, Y. Zhang, Suppression of vacancy cluster growth in concentrated solid solution alloys, Acta Mater. 125 (2017) 231–237.
41. Y.N. Osetskiy, L. Beland, A. Barashev, Y. Zhang, On the existence and origin of sluggish diffusion in chemically disordered concentrated alloys, Curr. Opin. Solid State Mater. Sci. 22 (2018) 65–74.
42. Y.N. Osetsky, L.K. Béland, R.E. Stoller, Specific features of defect and mass transport in concentrated fcc alloys, Acta Mater. 115 (2016) 364–371.
43. M.-R. He, S. Wang, S. Shi, K. Jin, H. Bei, K. Yasuda, S. Matsumura, K. Higashida, I.M. Robertson, Mechanisms of radiation-induced segregation in CrFeCoNi-based single-phase concentrated solid solution alloys. Acta Mater. 126 (2017) 182–193.
44. C. Lu, T. Yang, K. Jin, N. Gao, P. Xiu, Y. Zhang, F. Gao, H. Bei, Y. Dong, L. Wang, Radiation-induced segregation on defect clusters in single-phase concentrated solid-solution alloys, Acta Mater. 127 (2017) 98–107.

Table 1. Physical properties of Ni metal and equiatomic alloys of NiCo, NiFe, and NiCoFeCr. The melting temperatures (T_m) and the values of measured densities are taken from Ref [15]. Some electrical resistivity values, ρ(T), are from Refs. [7] and [16]. The measured total thermal conductivity (κ) at 300 K is taken from Refs. [7] and [16].

Metal/ alloys	Density ($g \cdot cm^{-3}$)[15]	Lattice (Å)	T_m (K)[15]	κ ($W\ m^{-1}\ K^{-1}$) at 5 K, 50 K[16] 300 K[7] and 973 K				ρ (μΩ cm) at 5 K, 50 K and 300 K[7]		
Ni	8.908	3.524	1728	≈280	328	88.0	67	≈0.1	0.16	7.8
NiCo	8.8484	3.535	1735	5.8	51.4	69.9	44	2.0	2.3	9.0
NiFe	8.2326	3.583	1703	1.7	15.4	28.0	25	10.3	11.0	36.5
NiCoFeCr	8.1445	3.572	1695	0.59	6.2	12.8	25	77.1	78.4	91.1

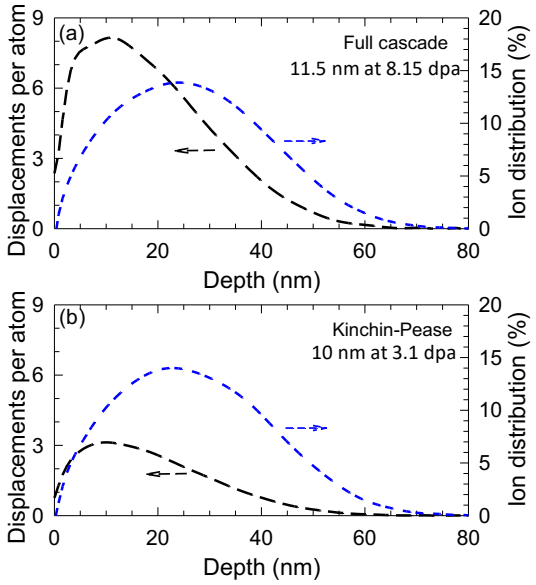

Fig. 1. SRIM predictions of 6 keV He implantation at 30° off the surface normal into NiFe to 6.0×10^{16} cm^{-2} based on (a) full-cascade or (b) quick (Kinchin-Pease) TRIM options.

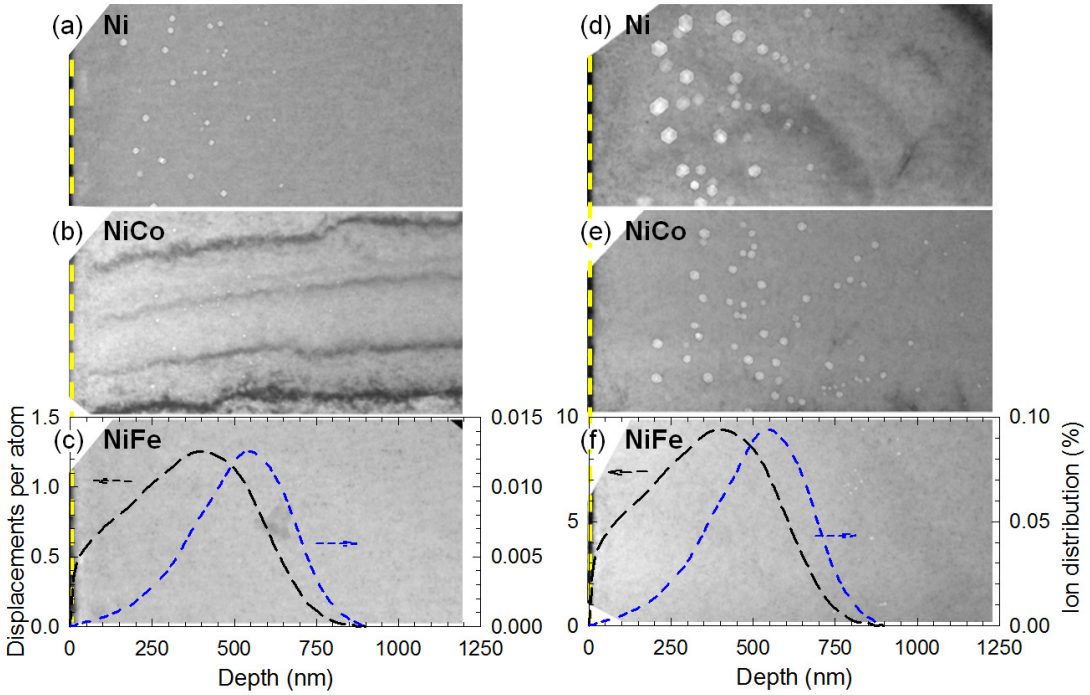

Fig. 2. Under-focused cross-sectional bright-field TEM images of Ni, NiCo, and NiFe irradiated by 1.5 MeV Ni^{+} at 500 °C to a fluence of 4×10^{14} (left) and 3×10^{15} cm^{-2} (right), respectively. Also overlaid on (c) and (f) are the SRIM-predicted dpa profile and injected Ni distribution from the full-cascade mode for the corresponding ion fluences

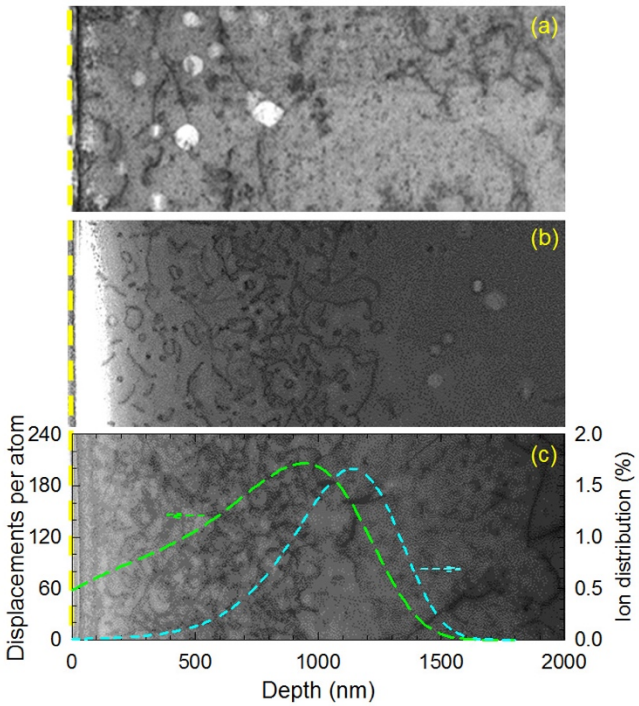

Fig. 3. On zone [110] BF-STEM images of Ni, $Ni_{0.8}Fe_{0.2}$, and NiFe irradiated by 3 MeV Ni^{+} at 500 °C to a fluence of 8×10^{16} cm^{-2}. Also overlaid on (c) are the SRIM-predicted dpa profile and injected Ni distribution from the full-cascade mode.

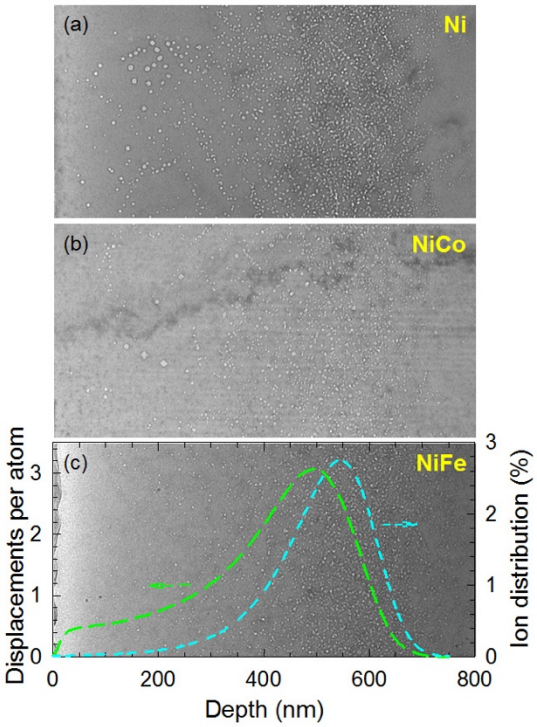

Fig. 4. Bright-field TEM images acquired at under-focused condition showing bubble distributions in Ni, NiCo, and NiFe implanted by 200 keV He ions at 500°C to a fluence of 5×10^{16} cm^{-2}. Also overlaid on (c) are the SRIM-predicted dpa profile and injected He distribution from the full-cascade simulation.

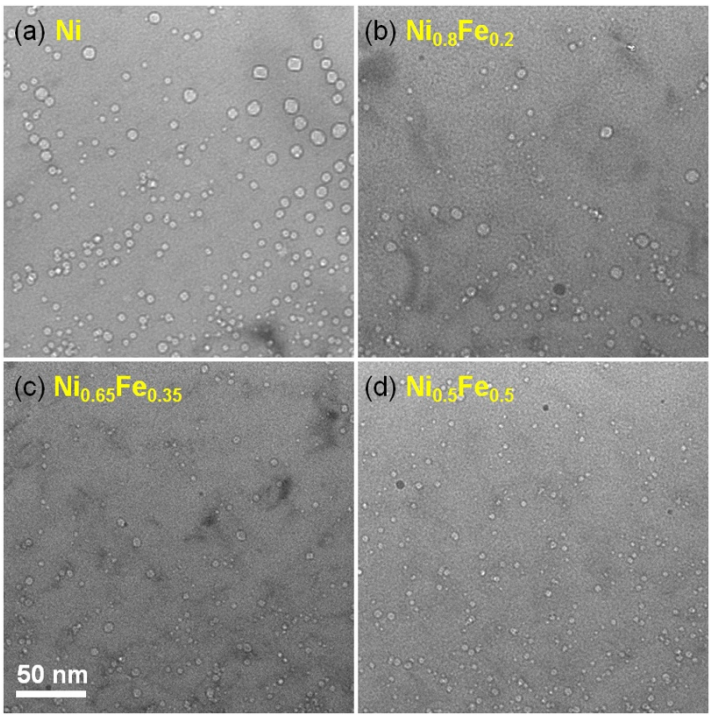

Fig. 5 TEM images of He bubbles in (a) Ni, (b) $Ni_{0.8}Fe_{0.2}$, (c) $Ni_{0.65}Fe_{0.35}$, and (d) $Ni_{0.5}Fe_{0.5}$(NiFe) acquired at under-focused condition in the region between 100 nm and 350 nm below the irradiated surface (a region that is relatively far from both the surface and the damage peak at 550 nm below the surface).

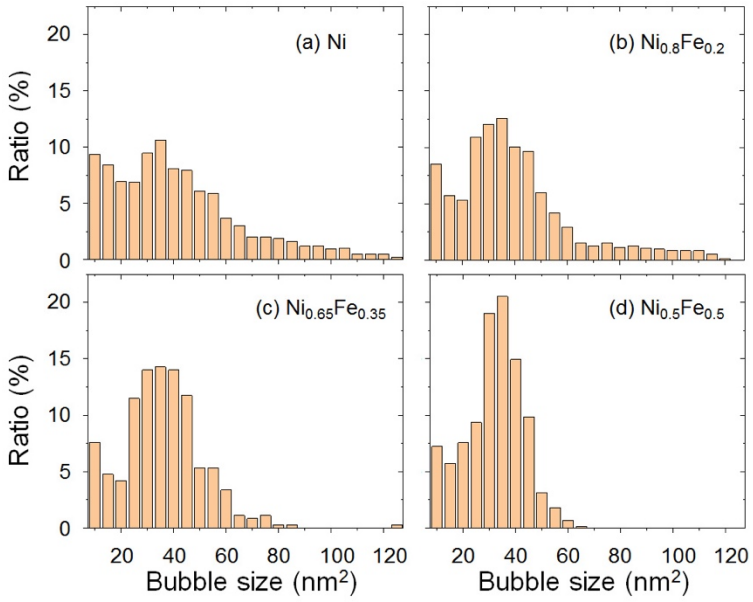

Fig. 6 Histograms showing the He bubble size distribution in (a) Ni, (b) $Ni_{0.8}Fe_{0.2}$, (c) $Ni_{0.65}Fe_{0.35}$, and (d) $Ni_{0.5}Fe_{0.5}$(NiFe) in a region between 100 nm and 350 nm below the surface.

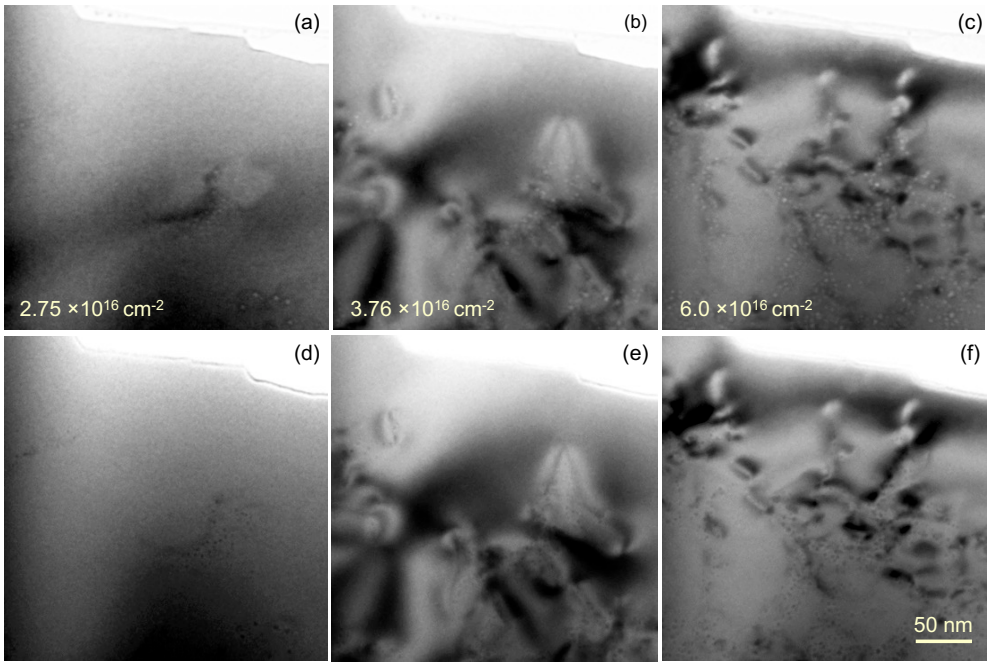

Fig. 7 In situ observation of cavity evolution under 6 keV He implantation in Ni. The images were taken at under- (top) and over- (bottom) focused conditions. The corresponding fluences are marked on the top images.

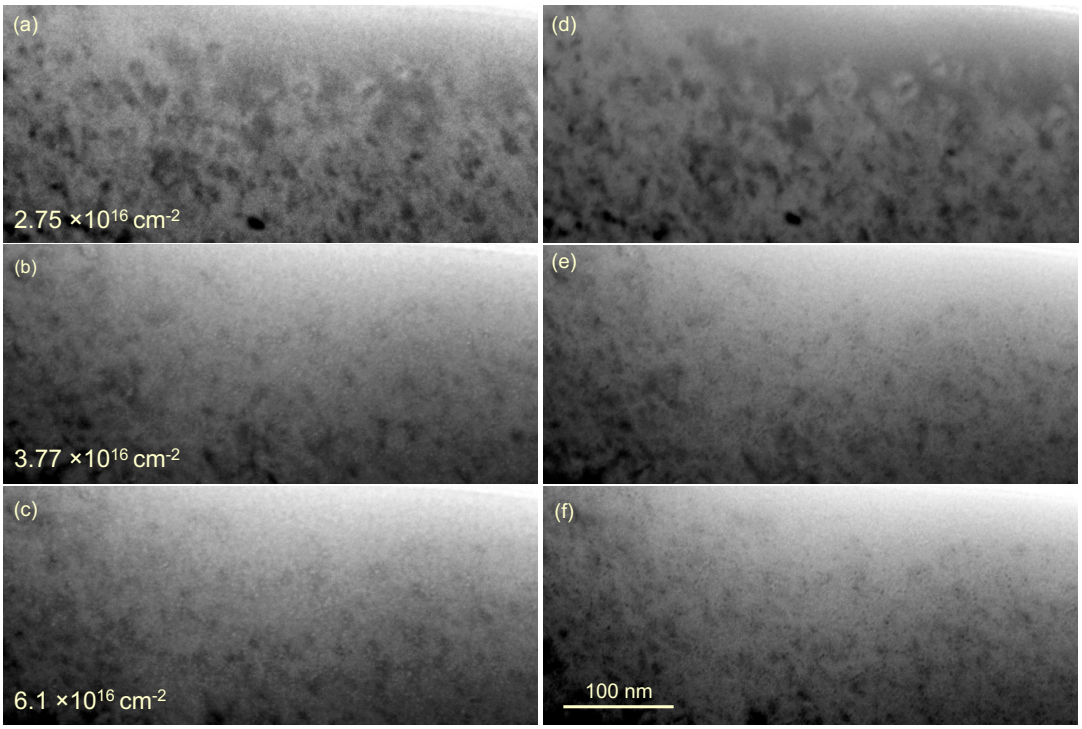

Fig. 8 In-situ observation of cavity evolution under 6 keV He implantation in NiCoFeCr. The images were taken at under- (left) and over-focused (right) conditions. The corresponding fluences are marked on the top images.

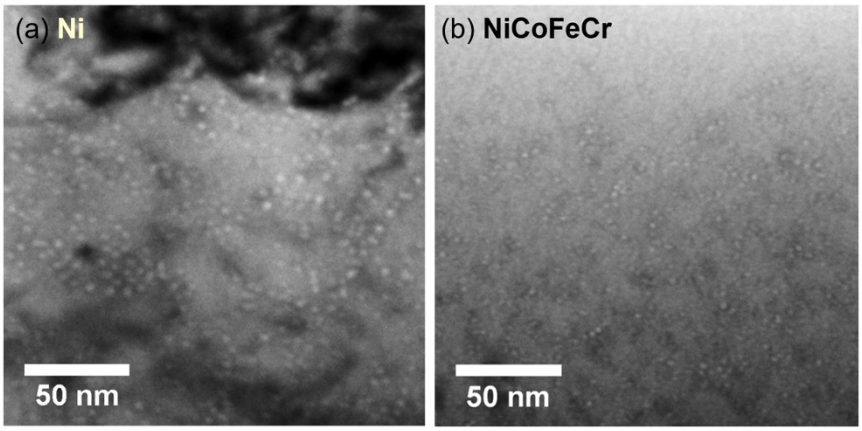

Fig. 9 Comparison of size of the He bubbles under 6 keV He implantation in (a) Ni to 6×10^{16} cm^{-2} and (b) NiCoFeCr to 6.1×10^{16} cm^{-2}.

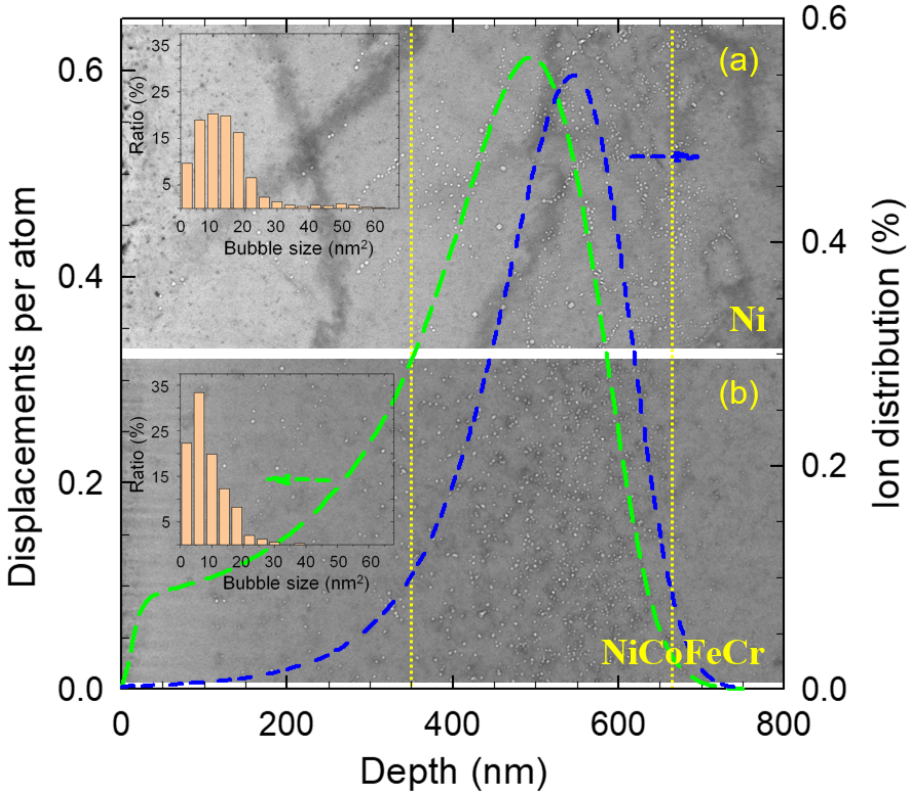

Fig. 10 Bright-field TEM images acquired at under-focused condition showing cavity distribution in (a) Ni and (b) NiCoFeCr under 200 keV He implantation at 500° to a fluence of 1×10^{16} cm^{-2}. The bubble size distributions are shown as insets accordingly. The SRIM-predicted dpa profile and injected He distribution from the full-cascade simulation are included.